INORGANIC CHEMISTRY FRONTIERS

RESEARCH ARTICLE

View Article Online
View Journal | View Issue



Cite this: *Inorg. Chem. Front.*, 2023, **10**, 4442

# Enhancing the nitrogen reduction activity of iron with inactive group-IVA elements at optimized stoichiometry†

Hanqing Yin,[a,b] Stuart Bell,[b,c] Dmitri Golberg [a,b] and Aijun Du *[a,b]

Received 30th April 2023,
Accepted 21st June 2023

DOI: 10.1039/d3qi00798g

rsc.li/frontiers-inorganic

Artificial ammonia synthesis is dominated by the Haber–Bosch (HB) process at present. Recently, concerns of huge energy consumption and air pollution from the HB process have created an increasing demand for economical and eco-friendly $NH_3$-synthesis approaches, such as electrocatalysis. Motivated by the fact that iron is widely used as a thermocatalyst in the HB process, we investigated bimetallic alloys consisting of Fe and group-IVA elements towards the electrochemical nitrogen reduction reaction (e-N2RR) *via* density functional theory calculations. Despite the inertness of pristine group-IVA elements towards the e-N2RR, alloying them with iron could surprisingly enhance the e-N2RR activity of iron. Moreover, we identified an optimal Fe–Si ratio (3 : 1) where a theoretical overpotential of only 0.21 V is observed, ranking among the best results ever. We also evaluated hydrogen evolution on $Fe_3Si$ and confirmed its low HER activity. Since most bimetallic alloys studied in this work have been synthesized, our work proposes a rational design for practical and economical e-N2RR electrocatalysts.



## 1. Introduction

Ammonia is one of the most irreplaceable raw materials in agriculture and chemical production,[1,2] thus making artificial ammonia synthesis a crucial process in both industry and economics. To date, the vast majority of artificially synthesized ammonia has come from the famous Haber–Bosch (HB) process where iron acts as the key component of the thermocatalyst.[3] However, the HB process is carried out under harsh conditions, costs a great deal of energy and induces environmental concerns due to the huge amount of carbon dioxide emission.[4,5] Exploring alternatives to the HB process is an urgent and significant topic for both engineers and researchers. Electrocatalysis is regarded as one of the promising methods because of the ambient reaction environment and sustainable electricity as the driving force, while products from electrochemical nitrogen fixation are also more environmentally benign compared with thermocatalysis.[6] Nevertheless, one of the key issues of the e-N2RR is the design of highly efficient catalysts which should effectively activate the $N_2$ molecule, decrease the energy barrier along the reaction pathway and possess a generally economical price. Therefore, searching for ideal candidates satisfying all these merits is a challenging yet rewarding task.

Metal-based compounds are always the first choices for catalyst design because they are more facile to be synthesized and more stable than some delicate nanostructures.[7,8] Some precious transition metal (TM) elements, including Ru,[9,10] Pd[11,12] and Nb,[13,14] are reported to be the most active components for e-N2RR, among which ruthenium is recognised as the best metal catalyst.[15] However, the high price of these elements is the bottleneck for their industrial application. To reduce the cost, some strategies were proposed to improve the usage efficiency of these precious metals. The first idea is to synthesize alloys consisting of both precious and non-precious elements. A lot of intermetallic compounds have been reported to be highly efficient catalysts for e-N2RR following this route. Jung's group synthesized Ru–Cu nanoparticles and performed an electrochemical test on the catalyst.[16] They observed a faradaic efficiency (FE) of 30.03% and a formation rate of 71.13 μg $h^{-1}$ $cm^{-2}$ towards ammonia. DFT calculations verified that the free energy change of the potential determining step (PDS) decreased after alloying Ru with Cu, resulting in an elevated activity. Yin *et al.* theoretically proposed a group of Ru-based ternary alloys as e-N2RR electrocatalysts on which the minimum theoretical overpotential is only 0.23 V.[17] Pang and co-workers prepared a nanoporous $Pd_3Cu$ alloy which restricts the competing hydrogen evolution reaction (HER) and has a

[a]*School of Chemistry and Physics, Queensland University of Technology, Gardens Point Campus, Brisbane, 4001, Australia. E-mail: aijun.du@qut.edu.au*
[b]*QUT Centre for Materials Science, Queensland University of Technology, Gardens Point Campus, Brisbane, 4001, Australia*
[c]*School of Mechanical, Medical and Process Engineering, Queensland University of Technology, Gardens Point Campus, Brisbane, 4001, Australia*
† Electronic supplementary information (ESI) available. See DOI: https://doi.org/10.1039/d3qi00798g

high yield-rate of 39.9 μg $h^{-1}$ $mg^{-1}$.[18] Some of the other similar alloy catalysts include $Pd_3Bi$,[19] PtMo[20] and $AuMo_3$ [21] whose details can be checked as referred. The second strategy is to disperse the precious metal down to the atomic scale, *i.e.*, the utilization of the popular single atom catalyst (SAC) concept.[22] Some of the noble-metal elements have been produced in the form of SACs towards the e-N2RR and their excellent performance could be maintained.[23–25]

Although the usage efficiency of precious metals can be greatly increased with the abovementioned strategies, it is still desired to achieve noble-metal-free catalysts for the e-N2RR to further reduce the cost and to explore new reaction mechanisms. Among non-noble transition metals, iron is undoubtfully the first choice because it is already used in the HB process, although the main reason for iron's wide application is its affordable cost while its catalytic activity is not very satisfying. One of the major approaches to boost the electrocatalytic performance of iron is still alloy engineering. Properties of pristine iron can be first modulated by alloying with other TM elements. Ahmed *et al.* synthesized a $CoFe_2O_4$ cluster supported by reduced graphene oxide sheets for the e-N2RR and observed an elevated performance compared with the monometallic Co and Fe.[26] Both cobalt and iron atoms can act as adsorption sites for $N_2$ so the density of active sites is greatly increased. Wang and co-workers produced Fe–Cu nanoclusters confined by carbon nanotubes and g-$C_3N_4$ and confirmed their enhanced activity towards the e-N2RR.[27] Duan and collaborators designed NiFe-nanomesh array as a bifunctional electrocatalyst for both the oxygen evolution reaction (OER) and the e-N2RR,[28] and the FE towards nitrogen reduction reached 12.5% at only 350 mV (*vs.* RHE). Other non-precious TM elements, such as Mo[29,30] and Zn,[31] have also been utilised to improve the activity of iron in the e-N2RR.

P-block elements have been recently found to play an intriguing role in electrochemical nitrogen fixation. They can either modify the property of TM elements by forming alloys[32,33] or directly act as the active centre.[34–36] Therefore, another large category of Fe-based electrocatalysts includes compounds constituted by iron and p-block elements. For example, iron and sulfur can form alloys with each other in different ratios in minerals, among which $FeS_2$[37,38] and 2D defective FeS[39] were proposed to capably catalyse the e-N2RR. Hou's group synthesized $FePS_3$ nanosheets with rich sulfur vacancies and reported excellent e-N2RR activity with a FE of 12.36%.[40] Chu *et al.* synthesized amorphous $FeB_2$ nanosheets and monitored a FE of 16.7% at −0.2 V.[41] Jin and co-workers developed a core–shell structure consisting of polypyrrole (PPy) coated S-doped $Fe_2O_3$ nanoparticles with a very-high FE of 26.4% towards the e-N2RR.[42] Although much progress has been made towards the application of iron-based materials to the e-N2RR, most of these works are conducted in labs while their delicate synthesis and feasibility on large scales are unclarified for practical applications.

Motivated by the above background and the prediction of uncommon above-room-temperature ferromagnetism in Fe–Si binary alloys,[43] we systematically investigated bimetallic alloys composed of iron and group-IVA elements with special attention on silicon *via* density functional theory simulations. We surprisingly found that Fe–Si binary alloys demonstrate excellent activity towards the e-N2RR. There is an optimal Fe : Si ratio (3 : 1) on which an overpotential of only 0.21 V can be achieved and this value is among the best reported results ever. The competing HER is also confirmed to be less selective because of the weaker adsorption of $H^+$ than $N_2$ and the unfavourable adsorption free energy of protons. In the case of Fe–Ge and Fe–Sn binary alloys, their performance is not so decent as their Fe–Si counterparts but is still better than the benchmarked Ru. Considering the successful synthesis of almost all candidates in this work and the low cost of iron and silicon, our work provided an economical and practical family of catalysts for the e-N2RR and illustrated the crucial role of p-block elements in the design of catalysts.

## 2. Computational details

All spin-polarized first-principles calculations were performed with the Vienna *ab initio* simulation package (VASP).[44,45] The projector augmented wave (PAW) method[46] was used to describe the ion–electron interaction and the Perdew–Burke–Ernzerhof (PBE)[47,48] form of exchange–correlation functional was applied as generalized gradient approximation (GGA). The energy cut-off for plane-wave basis sets was 400 eV while the convergence criteria for energy and force were $10^{-5}$ eV and $10^{-2}$ eV $Å^{-1}$, respectively. The Brillouin zones were sampled by 3 × 3 × 1 Monkhorst–Pack grids and the vdW interaction was corrected with a zero damping DFT-D3 method of the Grimme scheme.[49] Slab models of Fe–Si, Fe–Ge and Fe–Sn alloys were constructed with a thickness of around 10 Å. The bottom layers were fixed to mimic the bulk property while the upper layers were set free. The sizes of all computational cells were ensured to be large enough in the −*xy* direction and a vacuum layer of at least 16 Å in the −*z* direction was added to the models to separate adjacent cells.

To calculate the free energy change of each electrochemical step, the computational hydrogen electrode (CHE) model[50] was adopted as below:

$$\Delta G = \Delta E_{\mathrm{DFT}} + \Delta E_{\mathrm{ZPE}} - T\Delta S$$

where $\Delta E_{\mathrm{DFT}}$ is the electronic energy difference from standard DFT calculations, and $\Delta E_{\mathrm{ZPE}}$ is the modification of zero point energy which is obtained from the vibration energy of adsorbed intermediates. $T\Delta S$ is the entropic modification and $T$ was set to be 298 K. The ($\Delta E_{\mathrm{ZPE}} - T\Delta S$) term was calculated using the VASPKIT package.[51] The charge transfer between the $N_2$ molecule and the $Fe_3Si(001)$ surface was evaluated using the Bader charge analysis.[52]

## 3. Results and discussion

Before exploring Fe-IV group binary alloys, we need to revisit the catalytic performance of pristine iron to set a benchmark

criterion for Fe-based alloys within the same framework. According to previous works, the most active facets of iron in thermocatalysis are Fe(111) and Fe(211).[53] To confirm the performance of these two surfaces in electrocatalysis, we had a quick test by calculating the free energy change of $N_2$ adsorption and the first hydrogenation step as can be checked in Fig. S1.† It is clear that within the associative mechanism under electrochemical conditions, the Fe(111) surface suffers from a huge free energy barrier (~0.85 eV) of the first protonation step ($*NN + H^+ + e^- \rightarrow *NNH$) while the Fe(211) surface has a similar barrier (0.88 eV) for the same step, making them inefficient for the e-N2RR.

After clarifying the intrinsic activity of iron, we screened Fe-group-IVA bimetallic alloys of different stoichiometries within a reasonable range from the Materials Project program.[54] Since group-IVA elements are intrinsically inert for nitrogen reduction, we only investigated those candidates whose doping percentage is less than or equal to one, as displayed in Fig. 1 with structures of some typical candidates. The "*" symbol ahead of each candidate means it has been experimentally reported. The calculated lattice parameter in this work is in good agreement with the previously reported results as shown in Table 1. We studied the Fe–Si binary system first and followed the sequence from a low to a high Si-doping percentage. The first candidate is $Fe_4Si$ which is unfortunately not synthesized but we still picked it as a representative of a low Si-doping percentage. The conventional cell of $Fe_4Si$ can be found in Fig. S2a† and we checked all three facets in the {100} family because the geometry of the $Fe_4Si$ conventional cell is anisotropic. The (100) and (010) surfaces were found to be inactive to the e-N2RR due to the poor $N_2$ adsorption as concluded in Table S1.† However, $N_2$ could stably adsorb on the $Fe_4Si(001)$ facet in a horizontal mode with an adsorption energy of −0.55 eV. Afterwards, nitrogen reduction could happen *via* the enzymatic mechanism and the free energy diagram is shown in Fig. S2b† where a limiting potential of 0.52 V is observed. This performance is quite decent compared with many other theoretical results reported before.[15,62–64]

The next candidate is $Fe_3Si$ which we would emphasize most throughout this work. $Fe_3Si$ has a cubic structure as shown in Fig. 1c and has been experimentally synthesized previously.[55] We picked the (100) surface as an example to demonstrate the excellent performance of $Fe_3Si$ towards the e-N2RR. Similar to $Fe_4Si$, $N_2$ tends to be adsorbed on the $Fe_3Si(100)$ surface *via* the horizontal mode as shown in Fig. 2a and the

**Table 1** Previously reported and calculated lattice constants of all Fe-based binary alloys in this work

| Lattice constant | Reported data (Å) | DFT result (this work, Å) |
|---|---|---|
| $Fe_4Si$ | N/A | $a = 2.97$; $b = 4.00$; $c = 18.80$ |
| $Fe_3Si$ | $a = b = c = 5.665$ (ref. 55) | $a = b = c = 5.550$ |
| $Fe_{11}Si_5$ | $a = b = c = 5.414$ (ref. 56) | $a = b = c = 5.515$ |
| $Fe_2Si$ | $a = b = 3.93$, $c = 4.84$ (ref. 57) | $a = b = 3.89$, $c = 4.79$ |
| FeSi | $a = b = c = 4.485$ (ref. 58) | $a = b = c = 4.407$ |
| $Fe_{13}Ge_3$ | $a = b = c = 5.763$ (ref. 59) | $a = b = c = 5.665$ |
| $Fe_3Ge$ | $a = b = c = 5.733$ (ref. 60) | $a = b = c = 5.666$ |
| $Fe_3Sn$ | $a = b = c = 3.82$ (ref. 61) | $a = b = c = 3.767$ |

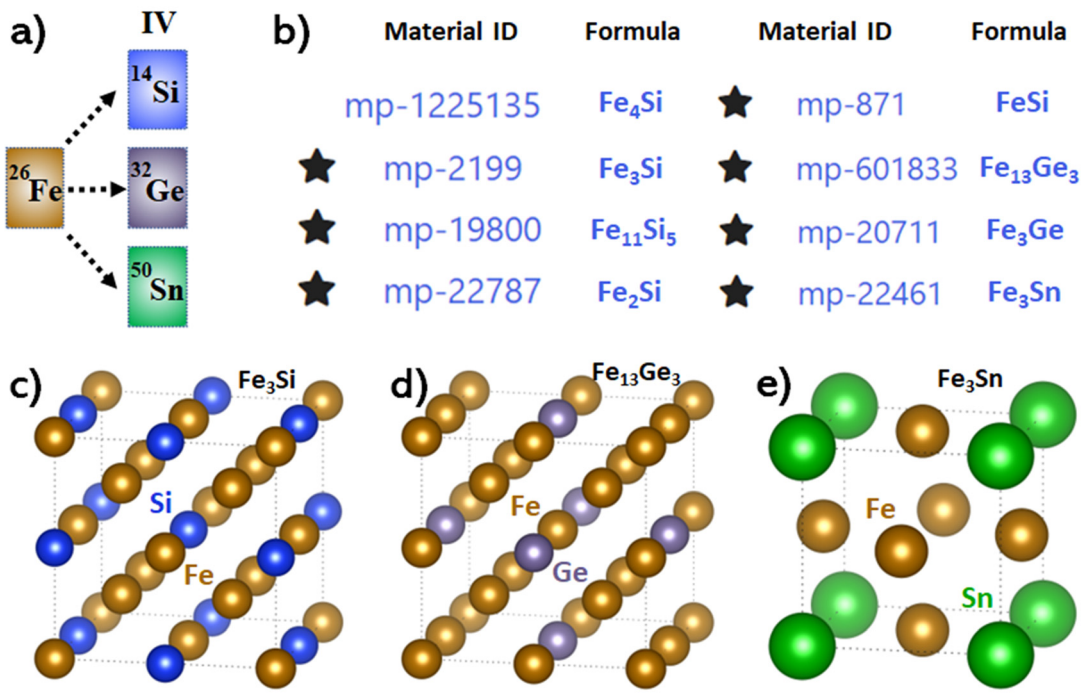


**Fig. 1** (a): Fe-group-IVA binary alloys studied in this work. (b): Eight candidates of Fe-group-IVA binary alloys with their IDs and formulas from the Materials Project database.[54] (c–e): Conventional cells of some typical atomic structures among all studied candidates.

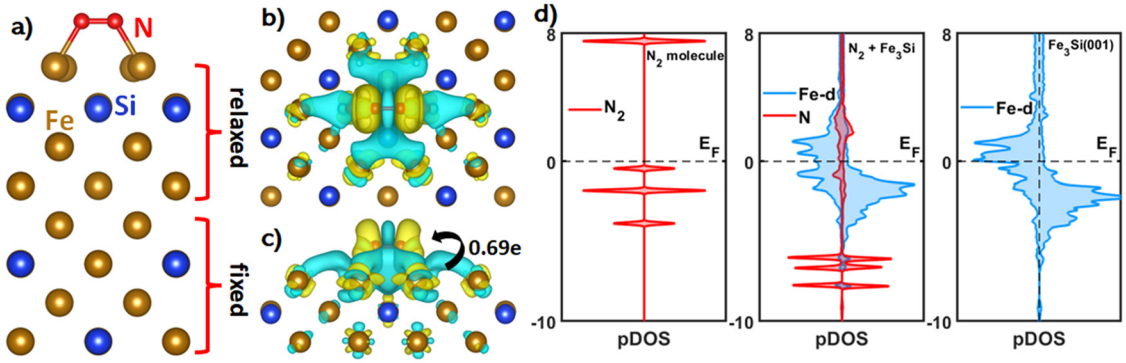


Fig. 2 (a): Horizontal mode of $N_2$ adsorption on the $Fe_3Si(100)$ surface. (b) and (c): Top and side views of the charge density difference plot of $N_2$ adsorption on the $Fe_3Si(100)$ surface. Yellow indicates charge accumulation and cyan represents charge depletion. The isosurface value is set to be 0.001 e $Bohr^{-3}$. (d): Projected density of states (PDOS) of isolated $N_2$, $N_2$ adsorbed $Fe_3Si$, and $Fe_3Si$.

adsorption free energy is −0.49 eV. To reveal the nature of such stable bonding, we performed charge density difference (CDD) and density of states (DOS) calculations and the results are shown in Fig. 2b–d. It is clear from the CDD plot that the triple bond of the $N_2$ molecule is effectively weakened due to the depletion of electrons, and a substantial $0.69e^-$ is transferred from the surface to $N_2$. The DOS results also indicated the interaction between the nitrogen molecule and the d-orbital of surface iron atoms near the Fermi level. Both results can clearly explain the stable adsorption of dinitrogen and prove that $N_2$ is activated for further electroreduction.

After clarifying the preferable $N_2$ adsorption mode, we studied the free energy evolution of the e-N2RR on $Fe_3Si(100)$ using the CHE model as shown in Fig. 3a. In general, $N_2$ might be reduced to $NH_3$ *via* either an associative or a dissociative mechanism. Nevertheless, a lot of theoretical works have proved that direct dissociation of the $N_2$ molecule is likely to occur in harsh environments while associative reduction accompanied by continuous hydrogenation is preferred under electrochemical conditions.[7,65,66] Therefore we only focused on the associative e-N2RR mechanism throughout this work. The horizontally adsorbed $N_2$ prefers the enzymatic pathway of the associative mechanism, in which protons attack both nitrogen atoms alternatively as shown in Fig. 3b. It has been previously proposed that the first and last hydrogenation steps are most probable to be the potential determining step (PDS) of the whole reaction process.[67] This is also the case of $Fe_3Si$ in which a positive free energy change of about 0.37 eV is observed and it is confirmed as the PDS corresponding to a theoretical overpotential of 0.21 V. It is worth noting that this value is among the lowest overpotentials ever reported. After the first protonation step, *N–*NH could be readily protonated to *NH–*$NH_2$ with two spontaneous steps with free energy changes of −0.14 eV and −0.30 eV, respectively. The free energy costs of the following steps are quite facile to be overcome until the production of two ammonia molecules. Extra calculations with an energy cutoff of 500 eV were also conducted and concluded in Table S2.† The controlled results showed negligible difference and proved that the original choice of 400 eV is sufficient to get an accurate outcome.

We also considered the selectivity towards $NH_3$ by investigating the competing HER on our $Fe_3Si$ catalyst as shown in Fig. S3.† The HER is a common parasitic reaction during the e-N2RR and it may significantly decrease the FE towards ammonia by generating unwanted $H_2$. From the computational point of view, the adsorption free energy ($\Delta G_H$) is a

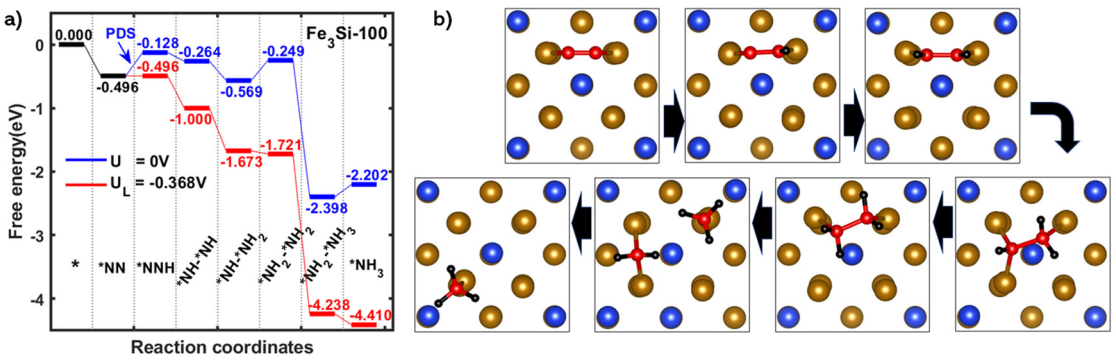


Fig. 3 (a): Free energy evolution of the e-N2RR on the $Fe_3Si(100)$ surface with PDS identified as the first protonation step. (b): Top views of adsorption configurations of all intermediates during the enzymatic pathway. Color map: bronze – Fe; blue – Si; red – N; and black – H.

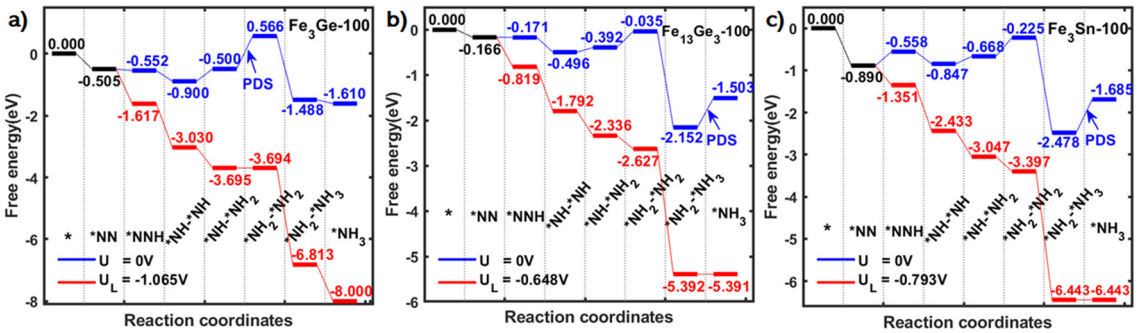


**Fig. 4** Free energy diagrams of electrochemical nitrogen reduction on (a) $Fe_3Ge$, (b) $Fe_{13}Ge_3$ and (c) $Fe_3Sn$, respectively. The best results among group-IV elements follow the sequence "Si > Ge > Sn".



good descriptor to evaluate the HER performance[68] and an ideal HER catalyst should possess "$\Delta G_H = 0$ eV". In fact, we analysed all possible sites for $H^+$ adsorption on the $Fe_3Si(100)$ surface and found the bridging site to be the most favourable adsorption site. The corresponding proton adsorption energy deviates a lot from the optimal value, suggesting poor HER performance. Meanwhile, since the adsorption energy of $N_2$ is larger than that of protons, we may also conclude that $N_2$ has an advantage over protons in competing for the adsorption site. Above all, both poor HER activity and preferable $N_2$ adsorption help steer the selectivity towards the e-N2RR instead of the HER on $Fe_3Si(100)$.

Now that we have got one candidate with an appropriate Fe–Si ratio that demonstrates excellent e-N2RR performance, it could be intriguing to further study Fe–Si binary systems with different atomic proportions. Since silicon is absolutely inert for the e-N2RR, we may deduce that a high percentage of Si-doping should deteriorate iron's activity. This deduction was verified to be true with our next candidate $Fe_{11}Si_5$, which has a cubic cell identical to that of $Fe_3Si$ but with one Fe atom replaced by a Si atom (Fig. S4a†). This small substitution difference elevates the largest free energy change in the whole process to about 0.63 eV which is much higher than that of $Fe_3Si$ as shown in Fig. S4b.† The next candidate, $Fe_2Si$, has a trigonal structure (Fig. S4c†) which is slightly more complex than the cubic structures of $Fe_3Si$ and $Fe_{11}Si_5$. We explored three different low-index facets of $Fe_2Si$ and found that a horizontal adsorption mode of $N_2$ would lead to a PDS free energy change of 0.92 eV as shown in Fig. S4d,† confirming the disadvantage of the excess silicon dopant. The last studied Fe–Si compound here is FeSi in which silicon possesses the same structural proportion as iron. It is found that the free energy changes of the first hydrogenation step for two different adsorption modes are both even larger than those of pristine Fe(111) and Fe(211) (Table S3†), preventing our further exploration of higher Si-percentages. To briefly summarize, we investigated five $FeSi_x$ ($0.25 \leq x \leq 1.00$) binary alloys for their performance towards catalysing the e-N2RR and obtained an ideal candidate ($Fe_3Si$) with excellent activity together with suppression of the competing HER.

Realising the positive role of Si in promoting the e-N2RR activity of iron, we extended the range to other group-IVA elements such as germanium and tin. For simplicity, we only picked those being experimentally synthesized and having the same or close doping percentage of 1/3, due to previous validation of $Fe_3Si$. These criteria lead to the choice of $Fe_3Ge$, $Fe_{13}Ge_3$ and $Fe_3Sn$. We investigated the energy evolution files on them following the same procedure as above and concluded the results as shown in Fig. 4. Among the three candidates, $Fe_{13}Ge_3$ has a limiting potential of 0.65 V and the value is 0.79 V for $Fe_3Sn$. As a general trend, the best results on Fe-group-IVA binary alloys follow the trend "Si > Ge > Sn" which is inversed as their atomic diameters.

## 4. Conclusions

Based on previous works where p-block elements were reported to play a positive role in enhancing the activity of TM-based catalysts, we studied existing Fe-group-IVA binary alloys towards e-N2RR by density functional theory calculations. We surprisingly found that inert silicon could substantially promote the catalytic activity of pristine iron. The activity of $FeSi_x$ alloys would initially increase with the addition of Si and then decrease if too much Si is alloyed with iron. The optimal Si-doping percentage was confirmed to be 1/3 and the theoretical overpotential on $Fe_3Si$ is only 0.21 V which is among the best reported results ever. The robustness against the HER on $Fe_3Si$ was also verified and the e-N2RR is favourable over the HER. The performance of several Fe–Ge and Fe–Sn bimetallic alloys was also briefly checked, and the best performances within both Fe–Ge and Fe–Sn families surpass the benchmarked Ru. Since most of the binary alloys listed here have been experimentally synthesized, our work proposes a category of practical and economical metal-based catalysts for e-N2RR. It might also provide a facile strategy for further experimental verification.

## Conflicts of interest

The authors declare that they have no known competing financial interests or personal relationships that could have appeared to influence the work reported in this paper.

## Acknowledgements

We acknowledge the generous offer of high-performance computer hours provided by NCI National Facility and the Pawsey Supercomputing Centre through the National Computational Merit Allocation Scheme (NCMAS) organised by the Australian Government and the Government of Western Australia. A. D. appreciates the funding from the Australian Research Council under Discovery Project (DP 210100721). D.G. is grateful to the ARC Laureate Fellowship (FL160100089).

## References

1 S. Licht, B. Cui, B. Wang, F.-F. Li, J. Lau and S. Liu, Ammonia synthesis by $N_2$ and steam electrolysis in molten hydroxide suspensions of nanoscale $Fe_2O_3$, *Science*, 2014, **345**, 637–640.

2 V. Rosca, M. Duca, M. T. de Groot and M. T. Koper, Nitrogen cycle electrocatalysis, *Chem. Rev.*, 2009, **109**, 2209–2244.

3 T. Wang and F. Abild-Pedersen, Achieving industrial ammonia synthesis rates at near-ambient conditions through modified scaling relations on a confined dual site, *Proc. Natl. Acad. Sci. U. S. A.*, 2021, **118**, e2106527118.

4 V. Kyriakou, I. Garagounis, A. Vourros, E. Vasileiou and M. Stoukides, An electrochemical haber-bosch process, *Joule*, 2020, **4**, 142–158.

5 L. Wang, M. Xia, H. Wang, K. Huang, C. Qian, C. T. Maravelias and G. A. Ozin, Greening ammonia toward the solar ammonia refinery, *Joule*, 2018, **2**, 1055–1074.

6 W. Qiu, X.-Y. Xie, J. Qiu, W.-H. Fang, R. Liang, X. Ren, X. Ji, G. Cui, A. M. Asiri and G. Cui, High-performance artificial nitrogen fixation at ambient conditions using a metal-free electrocatalyst, *Nat. Commun.*, 2018, **9**, 1–8.

7 X. Liu, Y. Jiao, Y. Zheng, M. Jaroniec and S.-Z. Qiao, Building up a picture of the electrocatalytic nitrogen reduction activity of transition metal single-atom catalysts, *J. Am. Chem. Soc.*, 2019, **141**, 9664–9672.

8 X. Duan, J. Xu, Z. Wei, J. Ma, S. Guo, S. Wang, H. Liu and S. Dou, Metal–free carbon materials for $CO_2$ electrochemical reduction, *Adv. Mater.*, 2017, **29**, 1701784.

9 E. Tayyebi, Y. Abghoui and E. Skulason, Elucidating the mechanism of electrochemical $N_2$ reduction at the Ru (0001) electrode, *ACS Catal.*, 2019, **9**, 11137–11145.

10 Y. Yao, H. Wang, X.-Z. Yuan, H. Li and M. Shao, Electrochemical nitrogen reduction reaction on ruthenium, *ACS Energy Lett.*, 2019, **4**, 1336–1341.

11 J. Wang, L. Yu, L. Hu, G. Chen, H. Xin and X. Feng, Ambient ammonia synthesis via palladium-catalyzed electrohydrogenation of dinitrogen at low overpotential, *Nat. Commun.*, 2018, **9**, 1–7.

12 S. Liu, Z. Wang, H. Zhang, S. Wang, P. Wang, Y. Xu, X. Li, L. Wang and H. Wang, Palladium nanothorn assembly array for efficient electroreduction of nitrogen to ammonia, *ACS Sustainable Chem. Eng.*, 2020, **8**, 14228–14233.

13 M. Zhang, H. Yin, F. Jin, J. Liu, X. Ji, A. Du, W. Yang and Z. Liu, Vacancy engineering of oxidized $Nb_2CT_x$ MXenes for a biased nitrogen fixation, *Green Energy Environ.*, 2022, DOI: **10.1016/j.gee.2022.01.010**.

14 R. Feng, H. Yin, F. Jin, W. Niu, W. Zhang, J. Liu, A. Du, W. Yang and Z. Liu, Highly Selective $N_2$ Electroreduction to $NH_3$ Using a Boron–Vacancy–Rich Diatomic Nb–B Catalyst, *Small*, 2023, 2301627.

15 S. Tang, Q. Dang, T. Liu, S. Zhang, Z. Zhou, X. Li, X. Wang, E. Sharman, Y. Luo and J. Jiang, Realizing a not-strong-not-weak polarization electric field in single-atom catalysts sandwiched by boron nitride and graphene sheets for efficient nitrogen fixation, *J. Am. Chem. Soc.*, 2020, **142**, 19308–19315.

16 C. Kim, J. Y. Song, C. Choi, J. P. Ha, W. Lee, Y. T. Nam, D. M. Lee, G. Kim, I. Gereige and W. B. Jung, Atomic–Scale Homogeneous Ru–Cu Alloy Nanoparticles for Highly Efficient Electrocatalytic Nitrogen Reduction, *Adv. Mater.*, 2022, 2205270.

17 H. Yin and A. Du, Revealing the Potential of Ternary Medium-Entropy Alloys as Exceptional Electrocatalysts toward Nitrogen Reduction: An Example of Heusler Alloys, *ACS Appl. Mater. Interfaces*, 2022, **14**, 15235–15242.

18 F. Pang, Z. Wang, K. Zhang, J. He, W. Zhang, C. Guo and Y. Ding, Bimodal nanoporous $Pd_3Cu_1$ alloy with restrained hydrogen evolution for stable and high yield electrochemical nitrogen reduction, *Nano Energy*, 2019, **58**, 834–841.

19 X. Wang, M. Luo, J. Lan, M. Peng and Y. Tan, Nanoporous intermetallic Pd3Bi for efficient electrochemical nitrogen reduction, *Adv. Mater.*, 2021, **33**, 2007733.

20 X. Guo, X. Li, Y. Li, J. Yang, X. Wan, L. Chen, J. Liu, X. Liu, R. Yu and L. Zheng, Molecule template method for precise synthesis of Mo-based alloy clusters and electrocatalytic nitrogen reduction on partially reduced PtMo alloy oxide cluster, *Nano Energy*, 2020, **78**, 105211.

21 J. L. Shi, S. Q. Xiang, D. J. Su, X. Liu, W. Zhang and L. B. Zhao, Theoretical Insights on Au–based Bimetallic Alloy Electrocatalysts for Nitrogen Reduction Reaction with High Selectivity and Activity, *ChemSusChem*, 2021, **14**, 4525–4535.

22 B. Qiao, A. Wang, X. Yang, L. F. Allard, Z. Jiang, Y. Cui, J. Liu, J. Li and T. Zhang, Single-atom catalysis of CO oxidation using Pt1/FeOx, *Nat. Chem.*, 2011, **3**, 634–641.

23 H. Tao, C. Choi, L.-X. Ding, Z. Jiang, Z. Han, M. Jia, Q. Fan, Y. Gao, H. Wang and A. W. Robertson, Nitrogen fixation by Ru single-atom electrocatalytic reduction, *Chem*, 2019, **5**, 204–214.

24 X. Wang, W. Wang, M. Qiao, G. Wu, W. Chen, T. Yuan, Q. Xu, M. Chen, Y. Zhang and X. Wang, Atomically dispersed Au1 catalyst towards efficient electrochemical synthesis of ammonia, *Sci. Bull.*, 2018, **63**, 1246–1253.

25 P. Shen, X. Li, Y. Luo, N. Zhang, X. Zhao and K. Chu, Ultra-efficient $N_2$ electroreduction achieved over a rhodium single-atom catalyst ($Rh_1/MnO_2$) in water-in-salt electrolyte, *Appl. Catal., B*, 2022, **316**, 121651.

26 M. I. Ahmed, S. Chen, W. Ren, X. Chen and C. Zhao, Synergistic bimetallic CoFe 2 O 4 clusters supported on graphene for ambient electrocatalytic reduction of nitrogen to ammonia, *Chem. Commun.*, 2019, **55**, 12184–12187.
27 X. Wang, S. Qiu, J. Feng, Y. Tong, F. Zhou, Q. Li, L. Song, S. Chen, K. H. Wu and P. Su, Confined Fe–Cu clusters as sub–nanometer reactors for efficiently regulating the electrochemical nitrogen reduction reaction, *Adv. Mater.*, 2020, **32**, 2004382.
28 Y. Sun, T. Jiang, J. Duan, L. Jiang, X. Hu, H. Zhao, J. Zhu, S. Chen and X. Wang, Two-dimensional nanomesh arrays as bifunctional catalysts for $N_2$ electrolysis, *ACS Catal.*, 2020, **10**, 11371–11379.
29 W. Liu, L. Han, H.-T. Wang, X. Zhao, J. A. Boscoboinik, X. Liu, C.-W. Pao, J. Sun, L. Zhuo and J. Luo, FeMo subnanoclusters/single atoms for neutral ammonia electrosynthesis, *Nano Energy*, 2020, **77**, 105078.
30 J. Wu, Z. Wang, S. Li, S. Niu, Y. Zhang, J. Hu, J. Zhao and P. Xu, $FeMoO_4$ nanorods for efficient ambient electrochemical nitrogen reduction, *Chem. Commun.*, 2020, **56**, 6834–6837.
31 L. Zhang, G. Fan, W. Xu, M. Yu, L. Wang, Z. Yan and F. Cheng, Isolated diatomic Zn–Fe in N-doped carbon for electrocatalytic nitrogen reduction to ammonia, *Chem. Commun.*, 2020, **56**, 11957–11960.
32 S. Guo, K. Heck, S. Kasiraju, H. Qian, Z. Zhao, L. C. Grabow, J. T. Miller and M. S. Wong, Insights into nitrate reduction over indium-decorated palladium nanoparticle catalysts, *ACS Catal.*, 2018, **8**, 503–515.
33 J. Yuan, H. Yin, X. Jin, D. Zhao, Y. Liu, A. Du, X. Liu and A. P. O'Mullane, A practical FeP nanoarrays electrocatalyst for efficient catalytic reduction of nitrite ions in wastewater to ammonia, *Appl. Catal., B*, 2023, **325**, 122353.
34 Q. Fang, H. Yin, X. Mao, Y. Han, C. Yan, A. P. O'Mullane and A. Du, Theoretical Evaluation of Highly Efficient Nitrate Reduction to Ammonia on InBi, *J. Phys. Chem. Lett.*, 2023, **14**, 2410–2415.
35 H. Yin, X. Mao, S. Bell, D. Golberg and A. Du, Transition-Metal-Free, Pure p-Block Alloy Electrocatalysts for the Highly Efficient Nitrate Reduction to Ammonia, *Chem. Mater.*, 2023, **35**, 2884–2891.
36 J. Crawford, H. Yin, A. Du and A. P. O'Mullane, Nitrate–to–Ammonia Conversion at an InSn–Enriched Liquid–Metal Electrode, *Angew. Chem.*, 2022, **134**, e202201604.
37 H. Du, C. Yang, W. Pu, L. Zeng and J. Gong, Enhanced electrochemical reduction of $N_2$ to ammonia over pyrite $FeS_2$ with excellent selectivity, *ACS Sustainable Chem. Eng.*, 2020, **8**, 10572–10580.
38 L. Gao, C. Guo, M. Zhao, H. Yang, X. Ma, C. Liu, X. Liu, X. Sun and Q. Wei, Electrocatalytic $N_2$ Reduction on $FeS_2$ Nanoparticles Embedded in Graphene Oxide in Acid and Neutral Conditions, *ACS Appl. Mater. Interfaces*, 2021, **13**, 50027–50036.
39 H. Yin and A. Du, Boosting Nitrogen Reduction Activity by Defect Engineering in 2D Iron Monochalcogenides FeX (X = S, Se), *Small Struct.*, 2022, **3**, 2200107.
40 H. Wang, Z. Li, Y. Li, B. Yang, J. Chen, L. Lei, S. Wang and Y. Hou, An exfoliated iron phosphorus trisulfide nanosheet with rich sulfur vacancy for efficient dinitrogen fixation and Zn-N2 battery, *Nano Energy*, 2021, **81**, 105613.
41 K. Chu, W. Gu, Q. Li, Y. Liu, Y. Tian and W. Liu, Amorphization activated FeB2 porous nanosheets enable efficient electrocatalytic N2 fixation, *J. Energy Chem.*, 2021, **53**, 82–89.
42 F. Jin, H. Yin, R. Feng, W. Niu, W. Zhang, J. Liu, A. Du, W. Yang and Z. Liu, Charge transfer and vacancy engineering of $Fe_2O_3$ nanoparticle catalysts for highly selective $N_2$ reduction towards $NH_3$ synthesis, *J. Colloid Interface Sci.*, 2023, **647**, 354–363.
43 Y. Niu, K. Zhang, X. Cui, X. Wu and J. Yang, Two-Dimensional Iron Silicide (FeSi x) Alloys with Above-Room-Temperature Ferromagnetism, *Nano Lett.*, 2023, **23**, 2332–2338.
44 G. Kresse and J. Hafner, Ab initio molecular dynamics for liquid metals, *Phys. Rev. B: Condens. Matter Mater. Phys.*, 1993, **47**, 558.
45 G. Kresse and J. Furthmüller, Efficient iterative schemes for ab initio total-energy calculations using a plane-wave basis set, *Phys. Rev. B: Condens. Matter Mater. Phys.*, 1996, **54**, 11169.
46 P. E. Blöchl, Projector augmented-wave method, *Phys. Rev. B: Condens. Matter Mater. Phys.*, 1994, **50**, 17953.
47 J. P. Perdew, J. A. Chevary, S. H. Vosko, K. A. Jackson, M. R. Pederson, D. J. Singh and C. Fiolhais, Atoms, molecules, solids, and surfaces: Applications of the generalized gradient approximation for exchange and correlation, *Phys. Rev. B: Condens. Matter Mater. Phys.*, 1992, **46**, 6671.
48 J. P. Perdew and Y. Wang, Accurate and simple analytic representation of the electron-gas correlation energy, *Phys. Rev. B: Condens. Matter Mater. Phys.*, 1992, **45**, 13244.
49 S. Grimme, Semiempirical GGA–type density functional constructed with a long-range dispersion correction, *J. Comput. Chem.*, 2006, **27**, 1787–1799.
50 J. K. Nørskov, J. Rossmeisl, A. Logadottir, L. Lindqvist, J. R. Kitchin, T. Bligaard and H. Jonsson, Origin of the overpotential for oxygen reduction at a fuel-cell cathode, *J. Phys. Chem. B*, 2004, **108**, 17886–17892.
51 V. Wang, N. Xu, J.-C. Liu, G. Tang and W.-T. Geng, VASPKIT: A user-friendly interface facilitating high-throughput computing and analysis using VASP code, *Comput. Phys. Commun.*, 2021, **267**, 108033.
52 W. Tang, E. Sanville and G. Henkelman, A grid-based Bader analysis algorithm without lattice bias, *J. Phys.: Condens. Matter*, 2009, **21**, 084204.
53 Q. An, M. Mcdonald, A. Fortunelli and W. A. Goddard III, Si-doped Fe catalyst for ammonia synthesis at dramatically decreased pressures and temperatures, *J. Am. Chem. Soc.*, 2020, **142**, 8223–8232.
54 A. Jain, S. P. Ong, G. Hautier, W. Chen, W. D. Richards, S. Dacek, S. Cholia, D. Gunter, D. Skinner and G. Ceder, Commentary: The Materials Project: A materials genome approach to accelerating materials innovation, *APL Mater.*, 2013, **1**, 011002.

 

55 N. Dahal and V. Chikan, Phase-controlled synthesis of iron silicide ($Fe_3Si$ and $FeSi_2$) nanoparticles in solution, *Chem. Mater.*, 2010, **22**, 2892–2897.
56 J. Wu, X. Chong, Y. Jiang and J. Feng, Stability, electronic structure, mechanical and thermodynamic properties of Fe-Si binary compounds, *J. Alloys Compd.*, 2017, **693**, 859–870.
57 Y. Sun, Z. Zhuo, X. Wu and J. Yang, Room-temperature ferromagnetism in two-dimensional Fe2Si nanosheet with enhanced spin-polarization ratio, *Nano Lett.*, 2017, **17**, 2771–2777.
58 Z. Chen, L. Wang, Q. Cheng, K. Zhang, X. Song, T. Mei, T. Yun and J. Dai, Selective synthesis and magnetic properties of iron silicide ($Fe_3Si$ and FeSi) at low temperature, *CrystEngComm*, 2022, **24**, 2748–2752.
59 M. Henriques, D. Berthebaud, A. Lignie, Z. El Sayah, C. Moussa, O. Tougait, L. Havela and A. Gonçalves, Isothermal section of the ternary phase diagram U–Fe–Ge at 900° C and its new intermetallic phases, *J. Alloys Compd.*, 2015, **639**, 224–234.
60 A. Erkisi and G. Surucu, The investigation DO3-type Fe3M (M = Al, Ga, Si and Ge) full-heusler alloys within first principles study, *Politeknik Dergisi*, 2018, **21**, 927–936.
61 The Materials Project. *Materials Data on $Fe_3Sn$ by Materials Project* 2022, DOI: 10.17188/1198303.
62 X. Liu, Y. Jiao, Y. Zheng and S.-Z. Qiao, Isolated boron sites for electroreduction of dinitrogen to ammonia, *ACS Catal.*, 2020, **10**, 1847–1854.
63 C. Choi, S. Back, N.-Y. Kim, J. Lim, Y.-H. Kim and Y. Jung, Suppression of hydrogen evolution reaction in electrochemical N2 reduction using single-atom catalysts: a computational guideline, *ACS Catal.*, 2018, **8**, 7517–7525.
64 Y. Abghoui, A. L. Garden, J. G. Howalt, T. Vegge and E. Skúlason, Electroreduction of N2 to ammonia at ambient conditions on mononitrides of Zr, Nb, Cr, and V: A DFT guide for experiments, *ACS Catal.*, 2016, **6**, 635–646.
65 J. Zhao and Z. Chen, Single Mo atom supported on defective boron nitride monolayer as an efficient electrocatalyst for nitrogen fixation: a computational study, *J. Am. Chem. Soc.*, 2017, **139**, 12480–12487.
66 C. Ling, Y. Zhang, Q. Li, X. Bai, L. Shi and J. Wang, New mechanism for N2 reduction: the essential role of surface hydrogenation, *J. Am. Chem. Soc.*, 2019, **141**, 18264–18270.
67 C. Ling, Y. Ouyang, Q. Li, X. Bai, X. Mao, A. Du and J. Wang, A general two–step strategy–based high–throughput screening of single atom catalysts for nitrogen fixation, *Small Methods*, 2019, **3**, 1800376.
68 J. K. Nørskov, T. Bligaard, A. Logadottir, J. Kitchin, J. G. Chen, S. Pandelov and U. Stimming, Trends in the exchange current for hydrogen evolution, *J. Electrochem. Soc.*, 2005, **152**, J23.